catalysts

MDPI

*Article*

# Photocatalytic-Fenton Process under Simulated Solar Radiation Promoted by a Suitable Catalyst Selection

**Aida M. Díez [1,*], Helen E. Valencia [2,3], Maria Meledina [2,3], Joachim Mayer [2,3] and Yury V. Kolen'ko [1]**

[1] Nanochemistry Group, International Iberian Nanotechnology Group, Avda. Mestre José Veiga s/n, 4715-330 Braga, Portugal; Yury.Kolenko@inl.int
[2] Central Facility for Electron Microscopy (GFE), RWTH Aachen University, D-52074 Aachen, Germany; valencia@gfe.rwth-aachen.de (H.E.V.); meledina@gfe.rwth-aachen.de (M.M.); j.mayer@fz-juelich.de (J.M.)
[3] Forschungszentrum Jülich GmbH, Ernst Ruska-Centre (ER-C), D-52425 Jülich, Germany
* Correspondence: adiez@uvigo.es

**Abstract:** Considering water scarcity, photo-based processes have been presented as a depollution technique, which should be optimized in order to be applied in the future. For that, the addition of an active photocatalyst and the usage of solar radiation are mandatory steps. Thus, $Fe_3O_4$–$SiO_2$–$TiO_2$ was synthesized, and its performance was evaluated using simulated solar radiation and methylene blue as a model pollutant. Under optimal conditions, 86% degradation was attained in 1 h. These results were compared to recent published data, and the better performance can be attributed to both the operational conditions selection and the higher photocatalyst activity. Indeed, $Fe_3O_4$–$SiO_2$–$TiO_2$ was physico-chemically characterized with techniques such as XRD, $N_2$ isotherms, spectrophotometry, FTIR, electrochemical assays and TEM.

**Keywords:** catalyst characterization; operational parameters; hydrogen peroxide; photo-Fenton; magnetic photocatalyst

**Citation:** Díez, A.M.; Valencia, H.E.; Meledina, M.; Mayer, J.; Kolen'ko, Y.V. Photocatalytic-Fenton Process under Simulated Solar Radiation Promoted by A Suitable Catalyst Selection. *Catalysts* **2021**, *11*, 885. https://doi.org/10.3390/catal11080885

Academic Editor: Giuseppina Iervolino

Received: 24 June 2021
Accepted: 15 July 2021
Published: 22 July 2021



## 1. Introduction

Photo-based processes have lately been presented as a treatment solution for polluted effluents, mainly thanks to the possibility of working with inexpensive solar radiation and its environmental friendliness [1–3]. However, in order to reduce the treatment times and to degrade non-photodegradable pollutants, a photocatalyst addition is mandatory.

This study applies the photocatalytic-Fenton-like process with a magnetic separable photocatalyst with visible activity ($Fe_3O_4$–$SiO_2$–$TiO_2$). It includes the most reported photocatalyst $TiO_2$ [4], magnetic $Fe_3O_4$ [5], which may also act as a photo-Fenton catalyst and $SiO_2$ in order to provide stability, avoid $Fe_3O_4$ interferences on $TiO_2$ and some of the drawbacks of the latter, such as low activity under solar radiation [6].

Thanks to $Fe_3O_4$, this photocatalyst can be magnetically separated from the bulb solution, thus it may avoid secondary pollution [5,7] without having to use heterogeneous photocatalysts, which are usually less performant [1,5,7].

Moreover, the iron presence can be used as a Fenton catalyst which generates more oxidant species (Equation (1)) [8]. Additionally, the $H_2O_2$ addition also favors the $TiO_2$ photocatalyst performance, as it avoids $e^-/h^+$ recombination thanks to its reaction with $e^-$ to produce HO· and $HO^-$ [2,9]. In this case, the radiation application is leveraged, as not only is it used for the $TiO_2$ photocatalysis, but also for the photo-Fenton process [10]. On this latter, the spent $Fe^{3+}$ (Equation (1)) is photo-reduced to $Fe^{2+}$, and also some complexes of iron with HO· and organic matter are photoactive, so they are broken by light radiation, allowing a higher content of $Fe^{2+}$, HO· and easily degradable organic matter. Thus, the performance of the photo-Fenton process is much higher than the Fenton process [8].

$$H_2O_2 + Fe^{2+} \rightarrow HO\cdot + HO^- + Fe^{3+} \quad (1)$$

The $Fe_3O_4$–$SiO_2$–$TiO_2$ catalyst was synthesized and characterized in order to explain its good performance on methylene blue (MB) degradation. This thiazine cationic dye has been widely reported [3,11,12] and the results can be compared to other studies, demonstrating $Fe_3O_4$–$SiO_2$–$TiO_2$ can compete with previously published data.

## 2. Results

### *2.1. Catalyst Performance*

To begin with, the efficiency of the synthesized catalyst was compared with the semiconductors it has within the structure, namely $TiO_2$ and $Fe_3O_4$ as well as the intermediate step of $Fe_3O_4$–$SiO_2$. For that, 3 g/L of $H_2O_2$ was added after a 60 min reaction. The synergistic effect of the semiconductor coupling on $Fe_3O_4$–$SiO_2$–$TiO_2$ catalyst can be seen on Figure 1. The effect of some parameters such as $H_2O_2$ dosage or MB dosage are depicted in Figures S3 and S4.

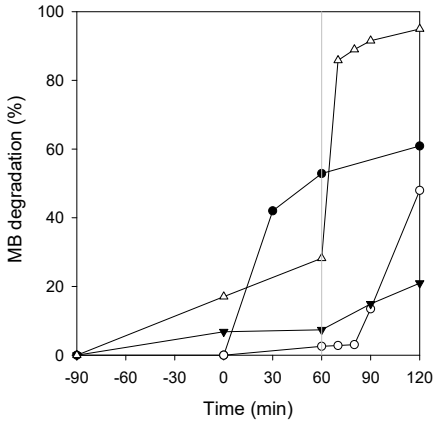


**Figure 1.** MB (20 mg/L) degradation in time with different catalysts (0.8 g/L): $TiO_2$ (black circles), $Fe_3O_4$ (white circles), $Fe_3O_4$–$SiO_2$ (black triangles), $Fe_3O_4$–$SiO_2$–$TiO_2$ (white triangles). The vertical grey line represents the moment of the $H_2O_2$ addition (3 g/L).

### *2.2. Catalyst Characterization*

Once $Fe_3O_4$–$SiO_2$–$TiO_2$ demonstrated a better photocatalytic activity, it was deeply characterized.

#### 2.2.1. TEM

High-angle annular dark field (HAADF) scanning transmission electron microscopy (STEM) measurement of the $Fe_3O_4$–$SiO_2$–$TiO_2$ material reveals spherical particles of approximately 280 nm in diameter, therefore, referred to as a nano-catalyst, see Figure 2A. In Figure 2B, a bright field (BF)-STEM image is depicted showing the surface of the nanocatalyst and highlighting crystalline grains of different orientations on the surface. Furthermore, energy-dispersive X-ray (EDX) measurements were performed in order to determine the elemental distribution throughout the particles, the elemental maps as well as the spectra are shown in Figure 2C to 2E. The core-shell structure is visualized in the elemental distribution map (Figure 2C): $SiO_2$ forms the silicon-rich core and is enveloped by a titanium-rich shell of $TiO_2$. The bight contrast in the upper part of the HAADF–STEM image could hereby be determined as Fe, see Figure 2D. The EDX spectrum (Figure 2E) with a subtracted background shows the elements present and reveals also the presence of Cu, which is known to appear due to the use of a Cu carbon film grid.

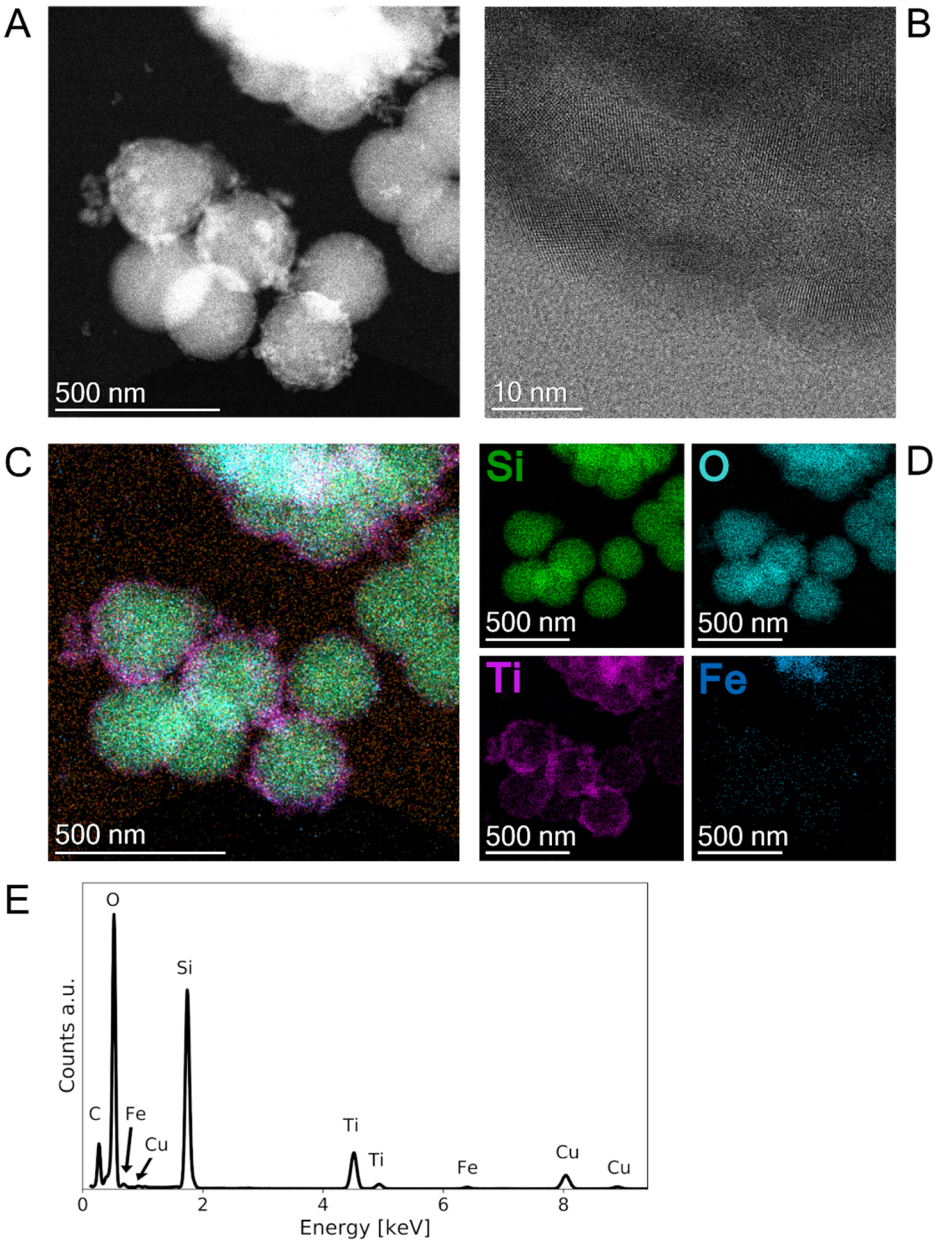


**Figure 2.** STEM of the $Fe_3O_4$–$SiO_2$–$TiO_2$ catalyst. (**A**) HAADF-STEM overview image, (**B**) BF-STEM zoom-in of the surface of one $Fe_3O_4$–$SiO_2$–$TiO_2$ particle. (**C**) EDX elemental map, (**D**) respective Ti, O, Si and Fe element distribution images and (**E**) corresponding spectrum of $Fe_3O_4$–$SiO_2$–$TiO_2$ catalyst.

### 2.2.2. Surface Area

The $N_2$ absorption–desorption isotherm is depicted in Figure 3. According to IUPAC classification, the isotherm is of type III where the isotherm increases quickly when reaching relative pressure close to unity. A small hysteresis loop appeared, indicating there are slight differences between the adsorption and desorption processes due to capillary condensation on the mesopores [13]. The hysteresis loop is of type H4, appearing between 0.6–0.9 of relative pressure, which indicates the presence of slit-like pores [13], maybe defined by the edges of the catalyst layers (Figure 2B). This indicates a mainly macroporous

structure. The obtained surface parameters are shown on Table S1, where it is remarkable that the small BET surface is of 29.127 $m^2/g$.

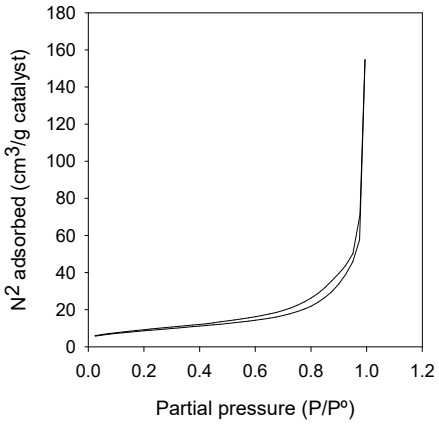


**Figure 3.** $N_2$ isotherm of the $Fe_3O_4$–$SiO_2$–$TiO_2$.

2.2.3. X-ray Diffraction

The successful catalyst synthesis is demonstrated by XRD measurement (Figure S5), where typical peaks of $TiO_2$ and $Fe_3O_4$ can be detected as it is explained in the supplementary material.

2.2.4. Fourier Transform Infrared

The FTIR spectra of $Fe_3O_4$–$SiO_2$–$TiO_2$ catalyst as well as the forming compounds are shown in Figure 4. The big vibration band related to $SiO_2$ can be noticed at 1100 $cm^{-1}$ whereas the $Fe_3O_4$ presence is related to the small bands at 900 $cm^{-1}$. $TiO_2$ presence is associated to the big band between 400 and 700 $cm^{-1}$ [6], covering also the Fe–O band which appears at 570 $cm^{-1}$ [12]. The intense peak at around 1070 $cm^{-1}$ is related to $SiO_2$ [14], indeed that big peak can be noticed in the samples which have this compound, demonstrating its presence and complementing previous XRD analysis.

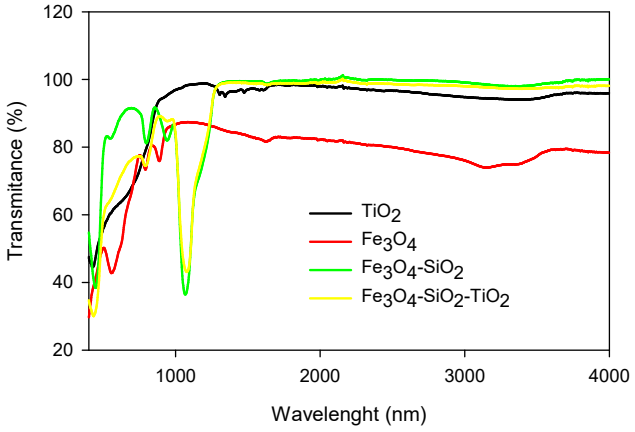


**Figure 4.** FTIR spectra of the $Fe_3O_4$–$SiO_2$–$TiO_2$ catalyst and the synthesis steps.

2.2.5. UV-VIS Spectra

The UV-vis spectra of the catalysts were measured, and the results are shown in Figure 5. As it can be seen, $Fe_3O_4$–$SiO_2$–$TiO_2$, $Fe_3O_4$ and $TiO_2$ show significant absorption bands at, respectively, 437, 560 and 400 nm. Following either Tauc's plot (embedded on the figures) or the formula $E_g = 1240/\lambda$, the band gaps are, approximately, 2.82 V for $Fe_3O_4$–

$SiO_2$–$TiO_2$, 2.15 V for $Fe_3O_4$ and 3.10 V for $TiO_2$. This makes the synthesized $Fe_3O_4$–$SiO_2$–$TiO_2$ catalyst to be active under simulated solar radiation.

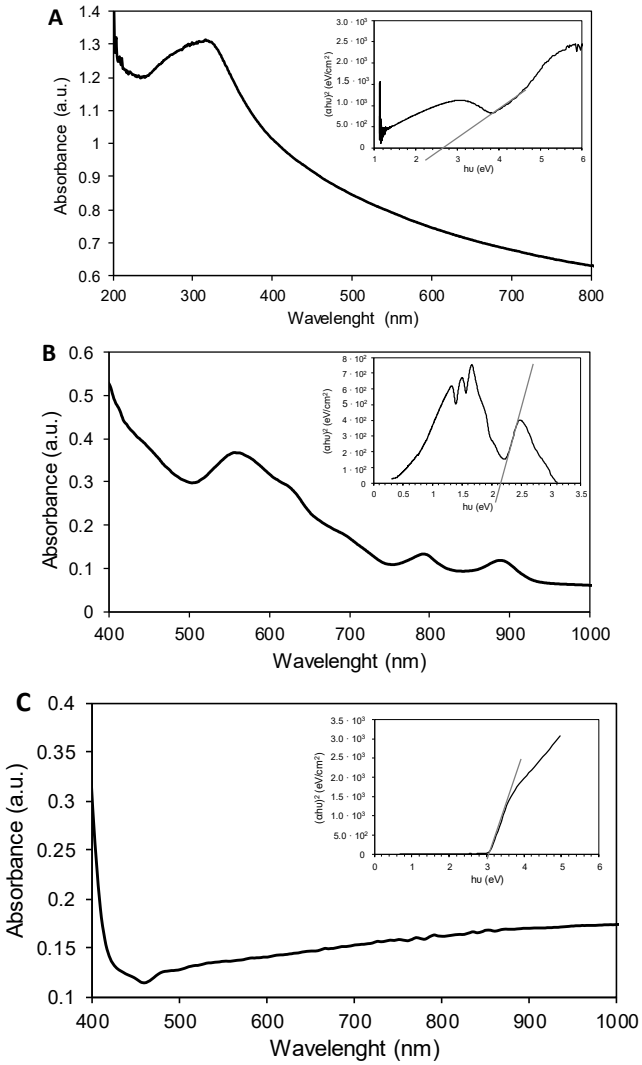


**Figure 5.** UV-Vis spectra and embedded Tauc's plots of (**A**) $Fe_3O_4$–$SiO_2$–$TiO_2$ catalyst (**B**) $Fe_3O_4$ and (**C**) $TiO_2$.

### 2.2.6. Electrochemical Properties

The electrochemical performance of the catalysts was measured by an electrochemical impedance spectroscopy and a cyclic voltammetry (CV) evaluation. The Nyquist plot confirms the changes in permittivity in terms of an increase in the conduction of the $Fe_3O_4$–$SiO_2$–$TiO_2$ catalyst when compared to $TiO_2$ (Figure 6).

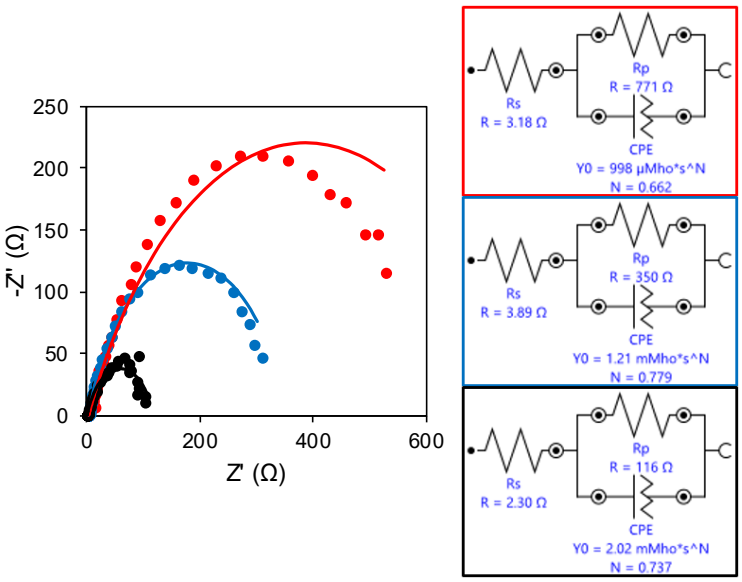


**Figure 6.** Nyquist data (dots) and equivalent circuit adjustment fit (line) on the left and simulated electrochemical circuit at right of $TiO_2$ (red), $Fe_3O_4$–$SiO_2$–$TiO_2$ (blue) and $Fe_3O_4$ (black) catalysts.

These results are in concordance with CV data. The higher CV performance has been related to an efficient photocatalytic performance [15]. Consequently, the higher performance of $Fe_3O_4$–$SiO_2$–$TiO_2$ (Figure S6), which is quite close to that of $Fe_3O_4$ when compared to $TiO_2$, indicates this latter catalyst may have a lower catalyst performance due to a fewer electron-hole separation capacity.

## 3. Discussion

### *3.1. Catalyst Performance*

The synthesized $Fe_3O_4$–$SiO_2$–$TiO_2$ catalyst works efficiently (Figure 1) for the photocatalytic-Fenton degradation of a MB polluted effluent due to the easiness of the generated radicals to attack $\pi$ bonds [16].

The $Fe_3O_4$–$SiO_2$–$TiO_2$ catalyst showed analogous performance under both UV and visible lamps, demonstrating a dual activity. This can be explained by the different adsorption peaks which are found in Figure 5A. Where a broad peak was detected between 400–500 nm, a slight absorption was also detected around 800 nm. Other authors have synthesized a dual activity photocatalyst such as graphene–$\alpha MoO_3$ nanocomposite, although that meant the necessity of higher treatment times (180 or 240 min) for the same pollutant [2].

The $Fe_3O_4$–$SiO_2$–$TiO_2$ showed a highly better activity when compared with the included semiconductors (Figure 1). Thus, its performance is widely better than $TiO_2$, $Fe_3O_4$ or $Fe_3O_4$–$SiO_2$. Out of the 95% degradation achieved, 20% was caused by adsorption on the particles, which took place during the first 90 min agitation under dark conditions. This confirms the theory that a good photocatalyst ensures a good absorption of the pollutant [2], favoring a much better degradation due to the proximity of the generated reactive species.

The higher performance of the $Fe_3O_4$–$SiO_2$–$TiO_2$ catalyst can be even maximized by the proper selection of the operational conditions. Thus, the treatment time was set at 60 min (Figure 1) and $H_2O_2$ and catalyst dosage at 0.6 and 0.8 g/L (Figures S3 and S4), respectively. Under these optimal conditions, 86.4% of MB degradation was attained in 1 h, which accounts for 1.41%/min, defeating previously reported data (Table 1), due to not only the usage of an active photocatalyst but also because of the influence of the operational parameters.

**Table 1.** Results for MB degradation attained during last year's photocatalysis processes (n.r.:not reported).

| MB (mg/L) | Radiation Source | $H_2O_2$ (mg/L) | Photocatalyst | | Elimination (%)/min | Ref. |
|---|---|---|---|---|---|---|
| | | | Type | Concentration (g/L) | | |
| 100 | Vis: 400 nm, 100 W | - | $TiO_2$–AC | 1 | 0.53 | [17] |
| 10 | Vis: 500 W | - | CuO/ZnO NPs | 2 | 0.71 | [18] |
| 3.19 | Vis: 420 nm, 300 W | - | $SrWO_4$/ $Bi_2O_3$ | 0.1 | 0.55 | [19] |
| 20 | Vis: n.r. | - | $Fe_3O_4$-ZnO–RGO | 0.25 | 0.56 | [12] |
| 10 | Vis: 400 nm | 0.16 | $CoFe_2O_4$ | 0.01 | 0.57 | [1] |
| 20 | Vis: 400–740 nm, 600 W. | 0.6 | $Fe_3O_4$–$SiO_2$–$TiO_2$ | 0.8 | 1.44 | This study |

3.1.1. Catalyst Dosage

Indeed, AlSalhi et al. [18] attained 0.71% degradation/min which was half when compared to this study (Table 1). Those authors also synthesized a coupled semiconductor catalyst (CuO/ZnO NPs) although they used 2 g/L, whereas this study fixed catalyst dosage at 0.8 g/L. Considering AlSalhi et al. used even less MB concentration and that it has been proven to favor the degradation performance (Figure S4A), the lower performance can be attributed to: (i) the usage of a less effective catalyst, which can be noticed on the UV-Vis spectra where the maximum absorption is found with a sharp 400 nm peak (compared to wider peaks in Figure 5A for $Fe_3O_4$–$TiO_2$–$SiO_2$) and the worse results in terms of Nyquist graphs (wider arcs) and higher electrochemical resistance; (ii) the fact that catalyst dosage is too high, provoking light scattering impeding the proper activation of the photocatalyst active sites [7].

On the other hand, if the catalyst dosage is not enough, fewer oxidant species are generated due to a lack of active centers to generate them [6]. This can be noticed when the results are compared to Subalakshmi et al. [19] who also used a coupled semiconductor ($SrWO_4$/$Bi_2O_3$) at a low concentration of 0.1 g/L. In this case, their synthesized photocatalyst does not show any absorption within the range 550–800 nm, providing a band gap of 3 eV. Nevertheless, they adapted this high band gap to a 420 nm cut-off lamp and thus, it is specific for their catalyst activation. Moreover, they used quite a low MB concentration. All of that indicates it is the catalyst dosage increase which could have favored MB degradation.

3.1.2. $H_2O_2$ Addition

Moreover, the results attained with the synthesized $Fe_3O_4$–$SiO_2$–$TiO_2$ catalyst defeat those attained with a similar catalyst ($Fe_3O_4$–ZnO–RGO) [12] (Table 1). This latter catalyst is also based on the coupling of (i) magnetic $Fe_3O_4$, (ii) a very good photocatalyst for UV, in their case ZnO instead of $TiO_2$ and (iii) reduced graphene oxide as a high surface support which is $SiO_2$ in our study. These authors could have increased the MB degradation with the addition of $H_2O_2$. Indeed, $H_2O_2$ addition enhances the process due to three factors: (i) the photo-decomposition of $H_2O_2$ can produce HO· which has a strong oxidizing capacity (2.8 V vs RHE) [16], (ii) the $e^-/h^+$ pairs can generate active radicals such as HO·, avoiding the $e^-/h^+$ recombination [3] and (iii) the $Fe^{2+}$ and $Fe^{3+}$ on the system lead to Fenton and Fenton-like reactions, favoring the generation of more radicals [1]. In this study, the more efficient concentration to work with was 0.6 g/L (Figure S3) due to the promotion of a higher generation of oxidants [10]. Nevertheless, increasing $H_2O_2$ too much makes the

efficiency to decrease due to its reaction with HO· to produce $HO_2$· which is less active than HO· [3]. On the other hand, small concentrations such as 0.16 mg/L used by Kalam et al. [1] with a $CoFe_2O_4$ catalyst may not be enough for the MB degradation as these authors attained a MB degradation of 0.57%/min (Table 1).

#### 3.1.3. Pollutant Concentration Effect

MB concentration has an important effect on the process performance (Figure S4A). Indeed, El-Salamony et al. [6] results performed worse (0.53%/min) than those attained in this study. This fact may be related to the higher (100 mg/L) pollutant concentration, although the lower lamp intensity used by those researchers (100 W vs. 600 W) may also affect the photo-degradation performance. However, these authors could have tested a proportional increase on catalyst dosage, and $H_2O_2$ if used, so the photocatalysis process maintains an almost stable performance (Figure S4B). The fact that MB concentration increase causes the efficiency to decay is related to light scattering due to a higher number of colorful molecules [6,7] and the fact that the photons interact with MB molecules (non-photodegradable) instead of the catalyst surface [11], making difficult the contact between the photocatalyst and photons [17].

On the other hand, reducing MB concentration increases the degradation performance (Figure S4A) due to a higher content of $H_2O_2$ and catalyst per molecule of MB, which promotes the given amount of HO· to be constant, and thus, when having less MB, those generated radicals can attack an elevated percentage of MB molecules [11]. This fact is demonstrated when $H_2O_2$ and catalyst dosage are reduced consequently, the MB degradation also drops, so the results are comparable to those attained at higher MB concentrations at the same ratio MB:$H_2O_2$:$Fe_3O_4$–$TiO_2$–$SiO_2$ (Figure S4B). This demonstrates that the effect of MB concentration is not a determinant factor and can be modified by a catalyst and $H_2O_2$ dosages.

Regarding Table 1 and $TiO_2$, $Fe_3O_4$ or $Fe_3O_4$–$SiO_2$ behavior (Figure 1), one can notice $Fe_3O_4$–$SiO_2$–$TiO_2$ performance is widely better for MB degradation. This higher performance can be explained by a deep catalyst characterization.

### *3.2. Catalyst Characterization*

The successful synthesis of the coupled catalyst can be confirmed by TEM and EDS, FTIR and XRD results (respectively, Figures 2 and 4, and Figure S5).

Regarding N2 isotherm type III (Figure 3), it is related to materials which have weak absorption characteristics [14], which may be positive for photocatalyst performance. Surface area is relatively small (Table S1), which can be explained by the blocking of some pores [6] of the containing materials due to the synthesis process. Nevertheless, a similar surface area of 29.69 $m^2/g$ has been reported as a sufficient surface area for promoting the absorption of active species and, thus, provoking a high catalytic activity [20].

On the other hand, the pore diameter is quite high (almost 4 nm) which accounts for the complexity of the catalyst which is synthesized in different layers [5] and which can be demonstrated in TEM images (Figure 2).

Considering the UV-Vis spectra (Figure 5), the $Fe_3O_4$–$SiO_2$–$TiO_2$ catalyst shows a shift which suggests a better absorption of UV-Vis radiation when compared to $TiO_2$, as the lower the band gap, the nearer visible region of the catalyst [13]. Indeed, the synthesized catalyst shows an experimental band gap of 2.82 V which favors the usage of the simulated visible lamp (400–740 nm).

Figure 6 shows Nyquist graphs and the simulated electrochemical circuits for $TiO_2$, $Fe_3O_4$ and $Fe_3O_4$–$TiO_2$–$SiO_2$ catalysts. Regarding the Nyquist plot, comparing $TiO_2$ and $Fe_3O_4$–$TiO_2$–$SiO_2$, the arc radius is highly decreased and that is related to a decrease on the charge transfer resistance [15,19]. Indeed, the linear part of the Nyquist plot at lower resistances is related to diffusion limited processes [21]. However, $Fe_3O_4$ seems to perform better, a fact explained by its stronger magnetic properties. Regarding the simulated circuits, the series resistance is related to the contribution of the electrode, which is why the

values are practically constant, whereas the parallel resistance is related to the layer resistance of the material [18] and one can notice the higher value attained for $TiO_2$ which is reduced to a half when using the synthesized $Fe_3O_4$–$SiO_2$–$TiO_2$ (350 Ω). The results indicate that both $Fe_3O_4$ and $Fe_3O_4$–$SiO_2$–$TiO_2$ have high conductivity and charge separation which is related to good catalytic activities [15,21]. Actually, $Fe_3O_4$–$SiO_2$–$TiO_2$ shows a higher resistance when compared to $Fe_3O_4$ due to the $TiO_2$ and $SiO_2$ addition which is performed to avoid the negative influence of the magnetic behavior of $Fe_3O_4$ on $TiO_2$ [5].

## 4. Materials and Methods

### *4.1. Reagents*

Different reagents were used for catalyst synthesis such as tetraethyl orthosilicate (TeOS) (98%, Sigma-Aldrich, Algés, Portugal), hydroxypropyl cellulose (15 mPa, 2% in water, Sigma-Aldrich), polyvinylpyrrolidone (MW of 29,000, Sigma-Aldrich), titanium butoxide (97%, Sigma-Aldrich), iron (III) chloride hexahydrate (99%, Acros Organics, Geel, Belgium) and iron (II) chloride tetrahydrate (99%, Sigma-Aldrich). Pure model pollutant MB was acquired from Sigma Aldrich. Milli-Q water was used for the experiences obtained from the Advantage A10 system (Merck, Algés, Portugal) (18.2 MΩ cm).

### *4.2. Catalyst Synthesis*

The catalyst was synthesized following subsequent steps. Briefly, magnetic $Fe_3O_4$ were synthesized following our previous published procedure [10] based on a co-precipitation method via the dropwise addition of 5 M NaOH using $FeCl_2$ and $FeCl_3$ (1:1.5) solution at 70 °C. Then, Chi et al.'s [5] procedure was used for the synthesis of $Fe_3O_4$–$SiO_2$ precursor. For that, 0.1 g of $Fe_3O_4$ particles were dispersed under sonication (1 h) in a mixture of 40 mL ethanol, 10 mL water and 1.1 mL of ammonia solution (30%). Then, TeOS was added dropwise under constant magnetic stirring which was left for 2 h. The product was collected by centrifugation and washed with deionized water. Then, the solid fraction was dried under vacuum at 50 °C.

For the $Fe_3O_4$–$SiO_2$–$TiO_2$ synthesis, 0.06 g of $Fe_3O_4$–$SiO_2$ particles were mixed under vigorous stirring with 0.24 mL of deionized water, 60 mg of ethanol and 0.1 g of hydroxypropyl cellulose. Once a homogeneous dispersion was attained, the temperature was increased to 85 °C and a mixture of titanium butoxide (0.2 mL) and ethanol (10 mL) was added to the previous dispersion and stirred for 90 min. The product was washed with ethanol several times, dried at 60 °C for 4 h and lastly calcined for 2 h at 500 °C (10 °C/min).

### *4.3. Set-Up*

The photocatalyst performance was assessed on a glass cylindrical reactor of 4 cm diameter and 6 cm height (50 mL capacity). It was placed under stirring (800 rpm) at 7 cm from the UV-Vis simulated lamp (400–740 nm, 600 W, from Toplanet, Madrid, Spain (Figure S1 in Supplementary material). Nevertheless, a preliminary test with the UV-led lamp (365 nm, 4.8 W, CMF-AR-A03, from Seoul viosys, Gyeonggi-do, Korea) was conducted in order to study the possibility of using low consumption lamps during night-time in a potential future usage. In order to avoid underestimating results, the photocatalyst was left for 90 min under stirring with the pollutant to attain adsorption equilibrium, with the lamp switched off. $H_2O_2$ addition was conducted after 60 min radiation, in order to roughly measure its effect as well as the $H_2O_2$ effect on the overall degradation. MB concentration was set at 20 mg/L, the catalyst dosage at 1.6 g/L and the $H_2O_2$ concentration at 3 g/L $H_2O_2$. Nevertheless, the process was studied deeply, and those values were, respectively, varied between 10–40 mg/L, 0–1.6 g/L and 0–6 g/L.

### *4.4. Analysis*

#### 4.4.1. Surface Area

For surface analysis, approximately 100 mg of sample were placed in the sample holder tube, and it was placed on the Autosorb iQ2 analyzer, Quantachrome (Florida, United States). The sample was degassed at 120 °C for 180 min. After that, the sample holder tube was placed into a liquid nitrogen bath (77.35 K) and the analysis was started. The specific surface area of the materials was determined by the Brunauer–Emmett–Teller (BET) method, and the total pore volume was calculated using the amount of vapor adsorbed at relative pressure close to unity ($P/P_0 = 0.97$) by assuming that the pores were filled with the liquid adsorbate, and thus, converting the adsorbed volume in volume of liquid $N_2$. The pore size distribution was estimated using the quenched solid density functional theory (QSDFT) approach for slit/cylindrical pores while treating the adsorption part of the isotherm.

#### 4.4.2. X-ray Diffraction

XRD analysis was conducted using X PERT PRO MRD from Pananalytical (Colorado, United States), measuring at an angular range between 20° and 80° 2ϴ degrees at a scan speed of 0.5°/min. Data was fitted with Cu–K$\alpha$ radiation ($\lambda$ = 1.5418 Å). Data were analyzed using the software Highscore (11.0, Pananalytical, Colorado, United States, 2020),

#### 4.4.3. Fourier Transform Infrared

FTIR was used for investigating the presence of functional groups and the co-ordination environment. Data were attained using the equipment Vertex 80v from Bruker (Massachusetts, United States) and data acquisition was conducted from 400 to 4000 nm under $N_2$ atmosphere.

#### 4.4.4. UV-Vis Spectra

The UV-Vis SpectroPhotoMeter (UV-2550, Shimadzu, Kyoto, Japan) was used to evaluate the optical behavior of the synthesized catalyst over the wavelength range 200–1000 nm. For that, 2 mm quartz cuvettes were used, and 0.05 g of catalysts were dissolved in ethanol. With those results, the energy gap ($E_g$) of the catalysts was calculated with Tauc's equation (Equation (2)).

$$(\alpha h\nu)^2 = A\,(h\nu - E_g)^n \quad (2)$$

where $\alpha$ is the absorption coefficient, h the Plank constant, ν the frequency, A the photon energy constant and n equals 2 [18].

The evaluation of the degradation process is related to the estrangement of the chromophore group [1] of MB and thus the degradation can be followed by the reduction in the area of the characteristic peak of MB (500–745 nm) (Figure S2).

#### 4.4.5. Electrochemical Characterization

The interfacial properties of the catalysts were evaluated by the electrochemical measurement of impedance and cyclic voltammetry using the PGSTAT302N Autolab (Metrohm, Herisau, Switzerland). For that, the catalyst was supported on 1 $cm^2$ Ni foam electrode (3 mg) after having prepared a solution (5 mg catalyst, 50 µL Nafion, 1 mL ethanol) which was added dropwise (up to 640 µL) to such electrode. Pt wire was used as a counter electrode and calomel electrode as a reference. The experiences were conducted in an electrolyte $Na_2SO_4$ 0.5 M (pH of 5.71) under constant stirring (600 rpm) where $N_2$ was bubbling to displace oxygen. The experiences were conducted with the used lamp switched on so it reproduces the behavior of the samples under visible activation. Specifically, impedance was measured at 1 V without stirring either magnet to avoid interferences.

4.4.6. TEM

The three powder samples were prepared on Cu carbon film grids and a probe-corrected STEM Hitachi HF5000 cold FEG electron microscope at 200 eV was used to acquire high-angle annular dark field (HAADF), bright field (BF) and secondary electron (SE) images. Together with two UltimMax TLE detectors from Oxford Instruments with a nominal collection angle of ~1.1 sr each for energy-dispersive X-ray (EDX) element mapping of the specimen (GFE, Aachen, Germany).

## 5. Conclusions

The $Fe_3O_4$–$SiO_2$–$TiO_2$ catalyst was successfully synthesized and demonstrated a good performance for the photocatalytic-Fenton degradation of MB under both UV and simulated solar radiation. For that, $H_2O_2$ (0.6 g/L) was used for activating both the photocatalysis and the photo–Fenton process, which happens simultaneously due to the coupled photocatalyst. The synthesized catalyst showed worthy properties such as good catalyst–pollutant interaction, low electrochemical resistance and wide visible absorption response, with a band gap of 2.82 V. Thus, the process was suitable for 86.4% degradation of 20 mg/L of MB in 1 h, defeating several recent studies due to different factors such as operational parameters discrepancies or the usage of a less active photocatalyst. Taking into account the well-performingt photocatalyst and the fact that the degradation is non-selective, this photocatalytic-Fenton process may be used for the treatment of other pollutants.

**Supplementary Materials:** The following are available online at www.mdpi.com/article/10.3390/catal11080885/s1, Figure S1: Fig. S1. Set-up schema. 1: Simulated visible lamp, 2: Cylindrical glass reactor, 3: Stirring bar, 4: Magnetic stirrer, Figure S2: Initial MB spectra attained by UV-Vis spectrophotometry, Figure S3: MB degradation at different $H_2O_2$ dosages: 6g/L (circles), 3g/L (asterisk), 1.5 g/L (triangles), 0.6 g/L (crosses), 0 g/L (rhombus). The vertical grey line represents the moment of the $H_2O_2$ addition, Figure S4: A: MB degradation at MB dosage of 10 ppm (white cycles), 20 ppm (triangles) and 40 ppm (black circles) with $H_2O_2$ 0.6 g/L and 0.8 g/L catalyst dosage B: MB degradation at same concentrations when keeping the ratio MB/$H_2O_2$ and MB/catalyst dosage at 0.025 and 33.33, respectively. The vertical grey line represents the moment of the $H_2O_2$ addition., Figure S5: XRD pattern of the synthesised $Fe_3O_4$-$SiO_2$-$TiO_2$ catalyst, Figure S6: Cyclic voltammetry of $TiO_2$ (red), $Fe_3O_4$-$SiO_2$-$TiO_2$ (blue) and $Fe_3O_4$ (black) catalysts.

**Author Contributions:** A.M.D.; formal analysis, A.M.D.; investigation, Y.V.K.; resources, A.M.D.; data curation, H.E.V.; TEM investigations, A.M.D.; writing—original draft preparation, A.M.D., Y.V.K. and M.M.; writing—review and editing, A.M.D.; visualization, J.M. and Y.V.K.; supervision, Y.V.K.; project administration, Y.V.K.; funding acquisition, Y.V.K. All authors have read and agreed to the published version of the manuscript.

**Funding**: The researcher Aida M. Díez is grateful to Xunta de Galicia for the financial support obtained (ED481B 2019/091). Helen E. Valencia wants to acknowledge the MEET-HiEnD III—Materials and Components to Meet High Energy Density Batteries with the funding number 03XP0258C and Maria Meledina recognizes the Verbundvorhaben iNEW: Inkubator Nachhaltige Elektro-chemische Wertschöpfungsketten with the funding number 03SF0589A for the funding.

**Acknowledges:** In this section, you can acknowledge any support given which is not covered by the author contribution or funding sections. This may include administrative and technical support, or donations in kind (e.g., materials used for experiments).

**Conflicts of Interest:** The authors declare no conflict of interest.

## References

1. Kalam, A; Al-Sehemi, A.G.; Assiri, M.; Du, G.; Ahmad, T.; Ahmad, I.; Pannipara, M. Modified solvothermal synthesis of cobalt ferrite ($CoFe_2O_4$) magnetic nanoparticles photocatalysts for degradation of methylene blue with $H_2O_2$/visible light. *Results Phys*. **2018**, *8*, 1046–1053.
2. Mahalingam S.; Ramasamy, J.; Ahn. Y.H. Synthesis and application of graphene-$\alpha MoO_3$ nanocomposite for improving visible light irradiated photocatalytic decolorization of methylene blue dye. *J. Taiwan Inst. Chem. Eng*. **2017**, *80*, 276–285.

3. Habib, I.Y.; Burhan, J.; Jaladi, F.; Lim, C.M.; Usman, A.; Kumara, N.T.R.N.; Tsang, S.C.E.; Mahadi, A.H. Effect of Cr doping in $CeO_2$ nanostructures on photocatalysis and $H_2O_2$ assisted methylene blue dye degradation. *Catal*. *Today* **2020**, 375, 506–513.
4. Homocianu, M., Pascariu, P. Electrospun Polymer-Inorganic Nanostructured Materials and Their Applications. *Polym*. *Rev*. **2020**, *60*, 493–541.
5. Chi, Y.; Yuan, Q.; Li, Y.; Zhao, L.; Li, N.; Li, X.; Yan, W. Magnetically separable $Fe_3O_4$@$SiO_2$@$TiO_2$-Ag microspheres with well-designed nanostructure and enhanced photocatalytic activity. *J*. *Hazard*. *Mater*. **2013**, *262*, 404-411.
6. El-Salamony, R.A.; Amdeha, E.; Ghoneim, S.A.; Badawy, N.A.; Salem, K.M.; Al-Sabagh, A.M. Titania modified activated carbon prepared from sugarcane bagasse: Adsorption and photocatalytic degradation of methylene blue under visible light irradiation. *Environ*. *Technol*. **2017**, *38*, 3122–3136.
7. Wang, S.; Gao, H.; Fang, L.; Hu, Q.; Sun, G.; Chen, X.; Yu, C.; Tang, S.; Yu, X.; Zhao, X.; Sun, G. Synthesis of novel CQDs/$CeO_2$/$SrFe_{12}O_{19}$ magnetic separation photocatalysts and synergic adsorption-photocatalytic degradation effect for methylene blue dye removal. *Chem*. *Eng*. *J*. *Adv*. **2021**, *6*, 100089.
8. Pignatello, J.J.; Oliveros, E.; MacKay, A. Advanced oxidation processes for organic contaminant destruction based on the Fenton reaction and related chemistry. *Crit*. *Rev*. *Environ*. *Sci*. *Technol*. **2006**, *36*, 1–84.
9. El-Naggar, M.E.; Wassel, A.R.; Shoueir, K. Visible-light driven photocatalytic effectiveness for solid-state synthesis of ZnO/natural clay/$TiO_2$ nanoarchitectures towards complete decolorization of methylene blue from aqueous solution. *Environ*. *Nanotechnol*. *Monit*. *Manag*. **2021**, *15*, 100425.
10. Diez, A.M.; Pazos, M.; Sanroman, M.A. Synthesis of magnetic-photo-Fenton catalyst for degradation of emerging pollutant. *Catal*. *Today* **2019**, *328*, 267–273.
11. Rahimi, S.M.; Arghavan, F.S.; Othmani, A.; Nasseh, N. Magnetically recoverable nickel ferrite coated with CuS nanocomposite for degradation of metronidazole in photocatalytic and photo fenton like processes. *Int*. *J*. *Environ*. *Anal*. *Chem*. **2020**, 1–21, doi:10.1080/03067319.2020.1817420.
12. Lei, Y.; Ding, J.; Yu, P.; He, G.; Chen, Y.; Chen, H. Low-temperature preparation of magnetically separable $Fe_3O_4$@ZnO-RGO for high-performance removal of methylene blue in visible light. *J*. *Alloys Compd*. **2020**, *821*, 153366.
13. Bardestani, R.; Patience, G.S.; Kaliaguine, S. Experimental methods in chemical engineering: Specific surface area and pore size distribution measurements-BET, BJH, and DFT. *Can*. *J*. *Chem*. *Eng*. **2019**, *97*, 2781–2791.
14. Mohamed, R.M.; Harraz, F.A. Photoreduction coupling of NiO/SiO2 nanocomposite with palladium and yttria nanoparticles: Visible-light-driven photocatalysts. *Mater*. *Res*. *Bull*. **2020**, *131*, 110965.
15. Pant, B.; Ojha, G.P.; Kuk, Y.S.; Kwon, O.H.; Park, Y.W.; Park, M. Synthesis and Characterization of ZnO-TiO2/Carbon Fiber Composite with Enhanced Photocatalytic Properties. *Nanomaterials* **2020**, *10*, 1960.
16. Doumic, L.I.; Génova, M.; Žerjav, G.; Pintar, A.; Cassanello, M.C.; Romeo, H.E.; Ayude, M.A. Hierarchically structured $TiO_2$-based composites for Fenton-type oxidation processes. *J*. *Environ*. *Manag*. **2019**, *236*, 591–602.
17. Saeed, M.; Ahmad, A.; Boddula, R.; ul Haq, A.; Azhar, A. Ag@MnxOy: An effective catalyst for photo-degradation of rhodamine B dye. *Environ*. *Chem*. *Lett*. **2018**, *16*, 287–294.
18. AlSalhi, M.S.; Sakthisabarimoorthi, A.; Devanesan, S.; Dhas, S.M.B.; Jose, M. Study on photocatalytic and impedance spectroscopy investigations of composite CuO/ZnO nanoparticles. *J*. *Mater*. *Sci*. *Mater*. *Electron*. **2019**, *30*, 13708–13718.
19. Subalakshmi, A.; Kavitha, B.; Srinivasan, N.; Rajarajan, M.; Suganthi, A. An affordable efficient $SrWO_4$ decorated $Bi_2O_3$ nanocomposite: Photocatalytic activity for the degradation of methylene blue under visible light irradiation. *Mater*. *Today Proc*. **2021**. in press
20. Guo, Y.; Zhang, J.; Zhou, D.; Dong, S. Fabrication of Ag/CDots/BiOBr ternary photocatalyst with enhanced visible-light driven photocatalytic activity for 4-chlorophenol degradation. *J*. *Mol*. *Liq*. **2018**, *262*, 194–203.
21. Mahanthappa, M.; Kottam, N.; Yellappa, S. Enhanced photocatalytic degradation of methylene blue dye using CuSCdS nanocomposite under visible light irradiation. *Appl*. *Surf*. *Sci*. **2019**, *475*, 828–838.